



## Photocatalytic and Oxygen Evolution Reaction (OER) of Novel Supercritical Fluid Synthesized Nanobiocomposite MoS<sub>2</sub>/Silk G

S. CHETANA<sup>1,\*</sup>, HALLIGUDRA GUDDAPPA<sup>2</sup>, SANJAY UPADHYAY<sup>3</sup>, NAVEEN CHANDRA JOSHI<sup>3</sup>, NIRAJ KUMAR<sup>3</sup>, PRIYVART CHOUDHARY<sup>4</sup> and VIKAS N. THAKUR<sup>5,\*</sup>

<sup>1</sup>Department of Mechanical Engineering, ATME College of Engineering, Mysore Kanakapura-Bangalore Road, Mysore-570028, India

<sup>2</sup>Department of Chemistry, ATME College of Engineering, Mysore Kanakapura-Bangalore Road, Mysore-570028, India

<sup>3</sup>Department of Physics, Rajadhani of College, University of Delhi, Delhi-110015, India

<sup>4</sup>Department of Biotechnology, School of Applied and Life Sciences, Uttaranchal University, Dehradun-248007, India

<sup>5</sup>Department of Electronics and Communication Engineering, Graphic Era Deemed to be University, Dehradun-248002, India

\*Corresponding authors: E-mail: chetana.s.mech@gmail.com; vikasnthakur92@gmail.com

Received: 13 November 2023;

Accepted: 8 January 2024;

Published online: 31 January 2024;

AJC-21531

The photocatalytic activity and oxygen evolution reaction (OER) of MoS<sub>2</sub> and silk graphene (silk G) composite synthesized using supercritical fluids and chemical vapor deposition (CVD) methods were investigated for their potential application in photocatalysis. This material was subjected to characterize by XRD, TEM, SEM and FTIR techniques to demonstrate that MoS<sub>2</sub>/silk G composite still existed in the supercritical fluids methods obtained MoS<sub>2</sub> & MoS<sub>2</sub>/silk G. The optical features of MoS<sub>2</sub> was improved by introduction of silk G, which in turn caused shift in band gap from 1.65 to 1.85 eV. Within visible region, creation of high electron-hole pairs is possible by adequate band gap modifications. The fast movement of photo-induced charge carrier can be enhanced by silk G as they decrease the recombination activity. Additionally, the MoS<sub>2</sub>/silk G shows high oxygen evolution reaction with low Tafel slope of 157.2 mV dec<sup>-1</sup> and low overpotential of 603 mV at a current density of 10 mA cm<sup>-2</sup>. The present study signifies that with addition of silk G in the MoS<sub>2</sub> host improved the photocatalytic activity by 13% and electrocatalytic activity by nearly 5% compared to bare MoS<sub>2</sub> nanoparticles.

**Keywords:** Oxygen evolution reaction, Silk graphene, Transmission electron microscope.

### INTRODUCTION

Applications for molybdenum disulphide (MoS<sub>2</sub>), a multi-layer transition metal chalcogenides material that looks graphite, include sensing, catalysis and batteries [1,2]. MoS<sub>2</sub> nanostructures have typically been synthesized by hydrothermal and gas-phase processes. There are evidences obtained from present study stating the remarkable performance of 2D MoS<sub>2</sub> modified electrodes in a polymer electrolyte membrane fuel cell as reaction catalyst for the oxidation-reduction which is platinum-free [3,4]. These electrodes comprise an extensive framework of modifying Mo and S atoms. Over the past few years, there has been a significant replacement of natural objects with chemical alternatives, as chemically derived products have become increasingly prevalent in our lives. While the numerous chemical goods make life easier for individuals, they also pollute our environment. For instance, a number of dyes and organic compounds that

makes water polluted were let out to rivers and other waterbodies by the chemical, pharmaceutical, artificial manufacturers, tropical applications sectors, etc. It is difficult to degrade these pollutants, which are harmful to the environment, however, getting rid of these pollutants is quite difficult.

Visible-light photodegradation technology has recently emerged as a viable strategy in the realm of environmental protection [5-7]. Several technologies such as photocatalysis, HER, OER, photo-Fenton, UV-H<sub>2</sub>O<sub>2</sub> and catalytic ozonation utilize renewable energy sources to efficiently degrade pollutants. Over the course of the past few years, catalysts related to transition metals have garnered a lot of attention due to the fact that they have an electronic structure that is similar to that of metals [8-12]. The energy required for almost perfect H<sub>2</sub> adsorption is present in MoS<sub>2</sub>, a typical transition metal dichalcogenide (TMD). Therefore, because of their usual availability, edge binding composition and outstanding catalytic activity,

they considered as powerful choice by water electrolysis [13]. However, due to its inferior electrical conductivity and decreased availability of proactive edge sites to the nano sheet stacking dissociation energy barrier, MoS<sub>2</sub> catalytic activity is severely constrained. Likewise, high-activated water to solve these shortcomings, a variety of techniques have been tried, including designing the crystallinity and morphology, linking heterogeneous materials, indicating increased active sites, promoting electron movement and lowering the initiated water dissociation energy barrier [14–18]. The majority of the materials utilized to decorate MoS<sub>2</sub> currently are 2D carbon compounds, which are noble metals. These materials have the potential to increase the co-catalytic activity of MoS<sub>2</sub>. Noble metals, on the other hand, are expensive and scarce on earth and metal oxides are susceptible to instability in acidic environments [19].

Several state-of-the-art oxidation methods for photocatalysis have been more important in technology over the past few years. Improved transformation advancements, including metal-air batteries, fuel cells and water electrolysis, are essential to this growth [20–22]. Nonetheless, to comprehend the advanced energy equipments however recognition of the underlying ideas, essentials and expertise of electrocatalysis is necessary. Electrochemical reactions on the surface of electrode materials can be sped up by a process called heterogeneous electrocatalysis. The water cycle and the carbon cycle are typically the two major energy cycles for energy related applications in electrocatalysis [7,23–27]. A number of electrocatalytic activities involving hydrogen and oxygen are crucial to the water cycle process. However, the contaminated water is frequently diaphanous and highly concentrated in multiple locations, which makes it challenging for light to flow through. Wastewater and photocatalysis have limited capacities [28]. As a result, it has, according to sources, the semiconductor based sonocatalysis has reportedly ex applications for dye removal benefit from a number of benefits thanks to ultrasonic technology. Any water medium can allow waves to exist and propagate. Given their high toxicity, endurance and refractoriness in the environment, organic contaminants have recently been the focus of a lot of environment friendly research [29].

Carbon-based nanomaterials are being used to increase the photocatalytic efficiency of semiconductors, including carbon nanotubes (CNTs) with band gaps of 0.5 eV, fullerenes having band gaps of 1.77 eV, graphene possessing zero band gaps and carbon nanofibers having band gaps of 0.7 eV [30]. Due to its tunable electrical properties and its ability to modify the surface active sites, we focused on reduced graphene oxide (rGO). Other carbon based compounds are expensive and difficult to synthesize in comparison to rGO. Molybdenum disulfide (MoS<sub>2</sub>), a p-type semiconductor, posses conventional 2D material structure where the covalent bonds amongst the Mo and S atoms create the S-Mo-S layer and the feeble van der Waals attraction interacts with the surrounding S-Mo-S structure. This unique layered structure can efficiently move reactants, intermediates and products from one layer to the next while allowing for high photo absorption of incoming sunlight through multiple reflections. Its structural features and the suitable band energy of 1.8 eV make it a good co-catalyst option [31,32]

Reduced graphene oxide (rGO) in combination with semi-conductors promotes electron dissociation and speeds up the breakdown of carcinogenic dyes caused by solar radiation. In this one-pot hydrothermal method for producing a hierarchical structure of nanosized MoS<sub>2</sub>/rGO [33]. In recent work, prepared MoS<sub>2</sub>/rGO composite sites' microstructure was studied. The characterization results show that the MoS<sub>2</sub> nanosheets may be anchored into and evenly distributed on rGO on both sides, which is advantageous for a well-ordered MoS<sub>2</sub> layer as opposed to unfavourable multilayer MoS<sub>2</sub> stacking. In particular, the template growth approach based on GO forms a hierarchical structure to offer a wide surface area and increase the efficiency of electrical conduction, in addition to expanding the inter-layers of MoS<sub>2</sub> and exposing a bigger percentage of the catalytically active sites. As a result, including GO in composition can increase the effectiveness of sonocatalysis conversion [34,35].

A straightforward, affordable and time-saving method for creating MoS<sub>2</sub> and silk G nanocomposite materials is provided in previous study [36]. Together with supercritical fluid (SCF) nanocomposites of silk G, MoS<sub>2</sub> was synthesized. A homogenous dispersion was produced by the easy intercalation of the charge transfer made possible by the silk G short size. The conductivity of silk G considerably increased when MoS<sub>2</sub> was added and these materials with larger conductivities had rising band gap characteristics. The MoS<sub>2</sub>/silk G composites exhibit effective degradation of methylene blue dye, displaying their compatibility with the environment, as biodegradable materials. The prepared composite shows high electrocatalytic interaction with oxygen resulting high cyclic stability.

## EXPERIMENTAL

**Synthesis of silk G (silk cocoon graphene):** The cocoons were mechanically crushed in a mortar and pestle before being pyrolyzed for 2 h at 400 °C in a tube furnace utilizing 3 g of ground Taser silk cocoon. The final black solid was collected under conventional conditions and utilized to retain raw carbon powder on Whatman filter paper. After washing raw carbon powder with petroleum ether followed by acetone, filter paper was used to filter the carbonized cocoon. Finally, brown mass was carefully washed with distilled water and preserved for further use.

**Silk graphene and MoS<sub>2</sub> composite synthesis:** MoS<sub>2</sub> 2D material was prepared by using 0.1 mL of hydrofluoric acid and ammonium heptamolybdate. Then 10 mL of deionized water was taken to disperse the above mixture and swirled continuously under normal conditions. Initially, the prepared MoS<sub>2</sub> material was put into a 10 mL stainless steel supercritical autoclave. This interaction was performed in the muffle furnace at 400 °C. The compound was collected from furnace and cooled in ice water after 30 min of interaction [37]. To remove the inorganic contaminations, the resultant material was repeatedly washed using ethanol and deionized water. To obtain a pure MoS<sub>2</sub> sample, centrifuged washed material was dried in a hot air oven at 60 °C for 12 h [38]. The composite sample was prepared using the same procedure by adding 100 mg of graphene from a silk cocoon to the precursor MoS<sub>2</sub>.

### Visible-light photodegradation of methylene blue dye:

The photocatalytic activity of synthesized MoS<sub>2</sub> and the MoS<sub>2</sub>/silk G of varied time were investigated under the 10 ppm methylene blue light and 250 W Xe arc lamp in addition to UV cut-off filter (400 nm) and a UV-Vis spectrometer. The intensity of the visible light was scattered upon the reaction solution and then measured. Following the standard procedure, four separate 100 mL methylene blue solutions having 10 ppm were prepared. Prior to introducing the photocatalytic nanocomposites, the optical density of aqueous methylene blue can be measured using a UV-Vis spectrophotometer, both in the absence of light and in the presence of freshly prepared aqueous methylene blue containing 50 mg of MoS<sub>2</sub> and 50 mg of MoS<sub>2</sub>/Silk G.

**Oxygen evolution reaction (OER) studies:** The electrochemical experiments were conducted using a Biologic EC lab SP-300 system, with a three-electrode cell configuration and 1 M KOH electrolyte solution. The working electrode preparation has been done using the same procedure as reported earlier [11]. In brief, synthesized sample (2 mg) was dispersed in ethanol having 150  $\mu$ L and later 20  $\mu$ L of Nafion-117 was added. The solution was ultrasonicated for 20 min and drop-wise coated on the nickel foam (1 cm  $\times$  0.5 cm). The prepared electrode was dried at 80  $^{\circ}$ C using hot air oven for 12 h. The platinum (Pt) paired with Ag/AgCl electrode were employed as counter and reference electrodes. Later, with 10<sup>-2</sup> to 10<sup>2</sup> Hz width of frequency was used for the evaluation of electrochemical impedance by spectroscopy (EIS). The significant results were modified to suit the reversible hydrogen electrode (RHE) according to the subsequent equation:

$$E \text{ (vs. RHE)} = E \text{ (vs. Ag/AgCl)} + E^{\circ} \text{ Ag/AgCl (reference)} + 0.0591 \text{ pH} \quad (1)$$

**Characterization:** The surface morphology and textures of silk G, MoS<sub>2</sub> nanoparticles and their composite were examined using an electron microscope (SEM) (ZEISS EVO 18). The phase and crystallographic data were determined by diffraction indications of X-ray utilizing XRD (Rigaku SmartLab2) and Raman spectroscopy (Thermo-Fisher DXR). Using the JEOL Japan JEM-2100 Plus, the HRTEM and SAED patterns of as-fabricated silk G, MoS<sub>2</sub> nanoparticles and their composite samples were examined. The EC Lab Biologic device was used for all electrochemical supercapacitor tests to measure the OER and EIS of synthetic sample-based electrode materials (Biologic VSP-3e) and also visible-light photodegradation studies identified by UV-VIS spectrophotometer (LABMAN LMSP-UV 1900) by home made visible-light photodegradation setup.

## RESULTS AND DISCUSSION

The XRD patterns of pure silk-graphene (silk G), pristine MoS<sub>2</sub> and MoS<sub>2</sub>/Silk G composite materials are shown in Fig. 1, respectively. In silk G sample, the distinctive broad peak was indexed at  $2\theta = 23.7^{\circ}$ , which indicate the amorphous nature. The principal distinctive peaks of pure MoS<sub>2</sub> sample were located at  $2\theta$  14.2 $^{\circ}$ , 33.6 $^{\circ}$ , 39.2 $^{\circ}$  and 58.1 $^{\circ}$ , respectively. These coordinates correspond to the (*hkl*) planes of (002), (100), (103) and (110) [39]. In both pristine and composite samples of silk

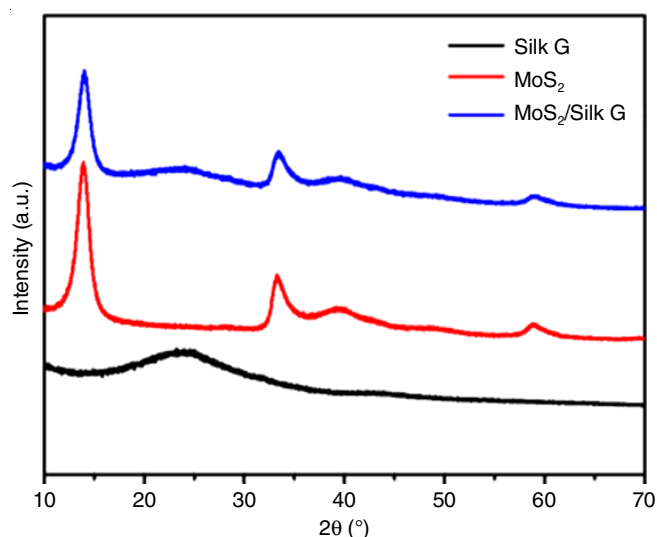


Fig. 1. XRD patterns of silk-based graphene (silk G), pristine MoS<sub>2</sub> (MoS<sub>2</sub>) and MoS<sub>2</sub>/Silk G nanobiocomposite

G/MoS<sub>2</sub>, a hexagonal MoS<sub>2</sub> crystal structure with a molybdenite phase has been identified. The MoS<sub>2</sub> sample had crystallographic characteristics of  $a = b = 3.190 \text{ \AA}$  and  $c = 14.879 \text{ \AA}$ , which matched the  $P6_3/mmc$ , 194 space group. The broad diffraction pattern of silk G at  $2\theta = 23.7^{\circ}$  and the similar major characteristics of pristine form of the silk G/MoS<sub>2</sub> composite sample, which correspond to the (*hkl*) (MoS<sub>2</sub>) of (002), (100), (103) and (110), respectively, confirmed the formation of silk G/MoS<sub>2</sub> composite without secondary phase formation or impurity.

Furthermore, the functional groups of silk G, MoS<sub>2</sub> and the MoS<sub>2</sub>/silk G composite were identified from FTIR spectroscopy. Spectrum obtained from FTIR of silk G (Fig. 2) reveals a band at 3448  $\text{cm}^{-1}$  as a result of O-H stretching. The stretching peak at 1650  $\text{cm}^{-1}$  is due to the presence of C=C, whereas the C-O stretching band appears at 1201  $\text{cm}^{-1}$ . It demonstrates that in contrast to silk G, the C-OH and C=O bonds in the elongated silk G disappears, which is due to the effective reduction of silk

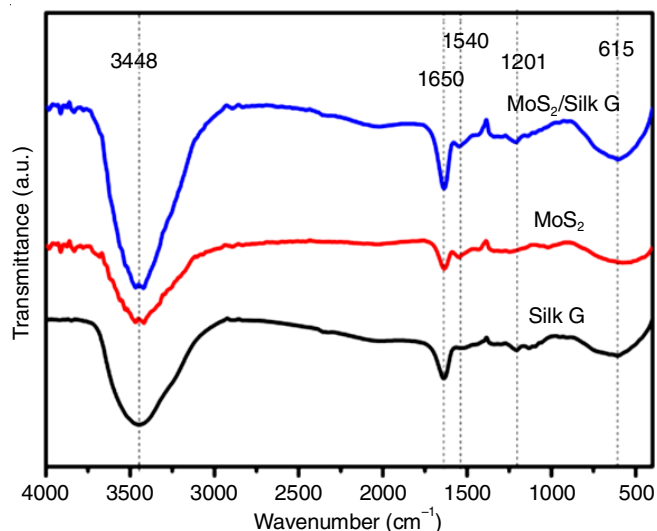


Fig. 2. FTIR spectra of silk-based graphene (silk G), pristine MoS<sub>2</sub> (MoS<sub>2</sub>) and MoS<sub>2</sub>/Silk G nanobiocomposite

G in the composite. The peak appears at  $620\text{ cm}^{-1}$  is attributed to the Mo-S stretching vibration, while the sulfate groups can be responsible for the several peaks at  $615\text{ cm}^{-1}$ . In contrast, absence of a C=O peak at  $1650\text{ cm}^{-1}$  shows that graphene has only undergone a minimal amount of oxidation [40]. Since silk G does not exhibit a peak in its XRD pattern, this accords support to that pattern. Interestingly, the intercalate related peaks for the MoS<sub>2</sub>/silk G composite exhibit a decrease in intensity, indicating that the intercalates have been removed from the interlayer structure as a result of the different surface chemistry between silk G and MoS<sub>2</sub>.

To further understand the formation process of silk G/MoS<sub>2</sub> composite, the Raman spectra of both the composite and pristine samples were analyzed (Fig. 3). The laser excitation at 488 nm was used to perform all of the Raman characterizations at room temperature. The main distinguished Raman bands in the silk G/MoS<sub>2</sub> composite have been appeared at  $271\text{ cm}^{-1}$  and  $428\text{ cm}^{-1}$ , which correlates to bands in pristine MoS<sub>2</sub> and simultaneously at  $1345\text{ cm}^{-1}$  and  $1400\text{ cm}^{-1}$  that indicates the distinctive silk G bands [41]. The fabrication of a silk G/MoS<sub>2</sub> composite was confirmed based on the Raman band positions and its structural features, which were consistent with previous investigations.

The neat silk-cocoon layers were folded with distinct and smooth surface textures and 2D morphology, as seen in the electron microscopic images of Fig. 4a-b. Figs. 4c-d and 4e-f illustrate the structures present on the surfaces of the MoS<sub>2</sub> sheets that were employed. Similarly, the surfaces of silk-G/MoS<sub>2</sub> sheets also exhibited the layered networks resembling those observed on MoS<sub>2</sub> sheets. The presence of Mo and S in the EDS spectra was confirmed by the composite sample at the same time, indicating that all elements were present with almost the requisite percentage composition.

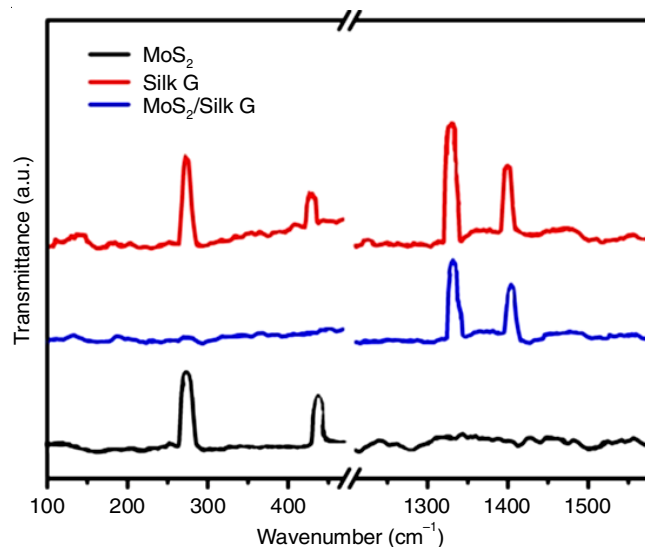


Fig. 3. Raman spectra of silk-based graphene (silk G), pristine MoS<sub>2</sub> (MoS<sub>2</sub>) and MoS<sub>2</sub>/Silk G nanobiocomposite

Fig. 5a-f displayed the transparent layered structure of the silk G sheet, while Fig. 5b-c clearly showed the heterojunction formed between synthesized MoS<sub>2</sub> layers and silk G sheet and forming silk G/MoS<sub>2</sub> composite. Fig. 5f indicated the HRTEM monographs of composite displaying the lattice fringes of the sample with interplanar spacings of 0.27 nm and 0.62 nm corresponding to the MoS<sub>2</sub> lattice. Carbon-based silk G is amorphous in nature and hence, in the SAED pattern (Fig. 5f) also, it can be observed that the SAED lattice planes are not visible in its composite structure.

The photocatalytic behaviour of MoS<sub>2</sub> and the MoS<sub>2</sub>/silk G composite was examined under ambient temperature using a

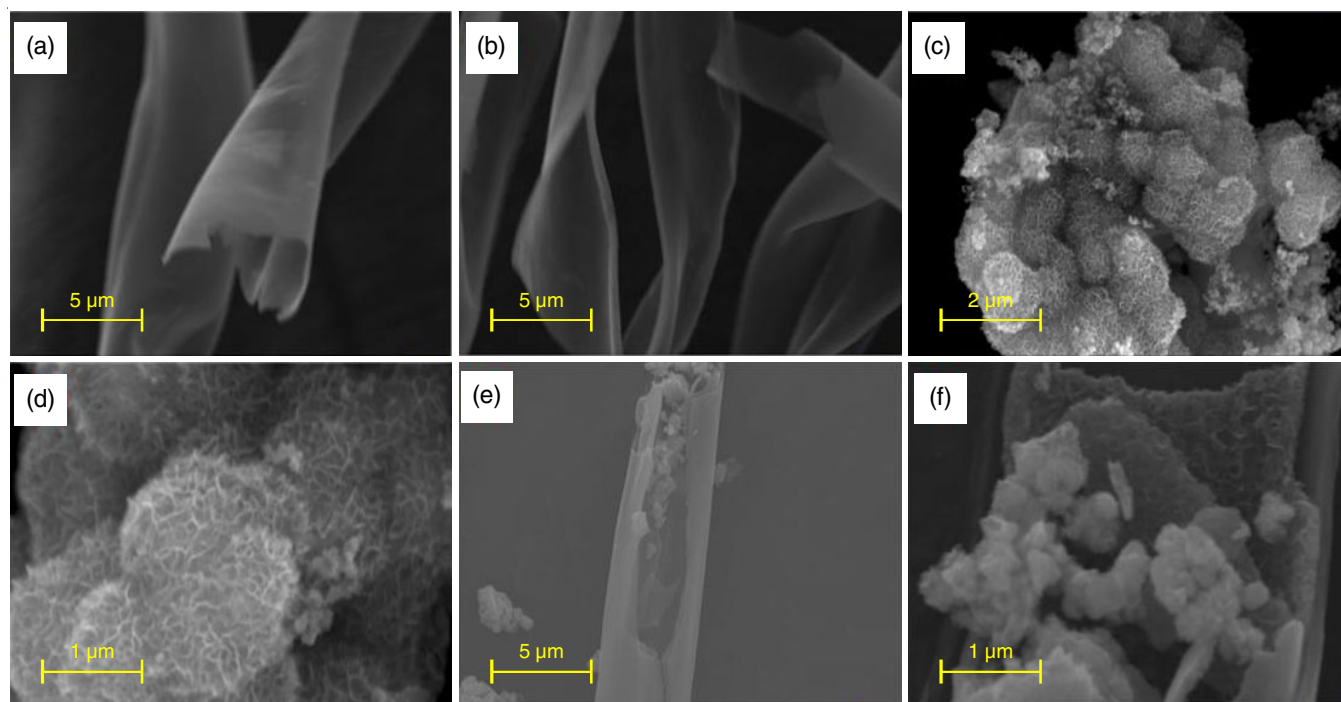


Fig. 4. (a,b) SEM micrographs of bare folded-silk cocoon layer, (c,d) SEM micrographs of MoS<sub>2</sub> layer, (e-f) SEM micrographs of MoS<sub>2</sub>/Silk G composite

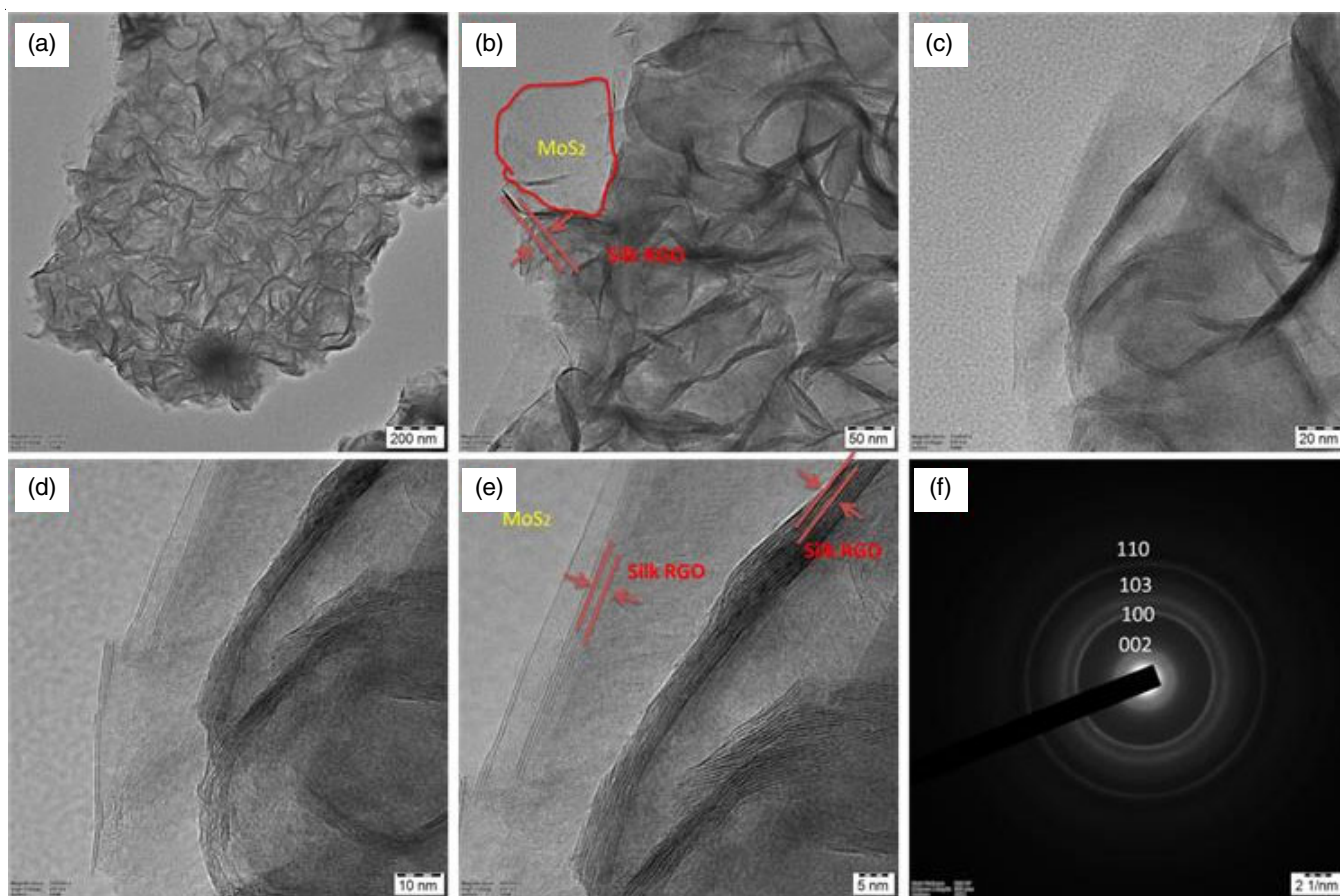


Fig. 5. (a-e) HRTEM images different magnification of MoS<sub>2</sub>/Silk G composite and (f) SAED pattern of MoS<sub>2</sub>/Silk G composite

250 W Xe arc lamp equipped with a UV dissociated filter (400 nm) and a UV-Vis spectrometer. The standard approach involved the preparation of four different 100 mL aqueous methylene blue (10 ppm) dye solutions. A UV-Vis spectrophotometer was used to measure the absorbance of aqueous methylene blue solution before the addition of photocatalytic nanocomposite (Fig. 6b-c). In dark condition, a solution containing 50 mg of MoS<sub>2</sub> and 50 mg of MoS<sub>2</sub>/silk G was prepared by dissolving them in aqueous methylene blue solutions that were freshly prepared. To achieve the equilibrium of adsorption-desorption, this mixture was shaken rigorously for 30 min. The pH of aqueous suspension was measured and found to be 7.2. Prior to the sample being analyzed with a UV-Vis spectrophotometer, each beaker was filled with a solution mixture that was approximately 5 mL in volume and then centrifuged. This suspension was additionally exposed to visible light while being continuously stirred to assess the photocatalytic reaction at different interval of time periods (10, 20, 30, 40, 80, 100 and 120 min) and results of their absorbance were analyzed from UV-Vis analysis (Fig. 6b-c).

Absorption of visible light by these materials resulted in the production of a single electron pair, surpassing the bandgap of 1.6 eV as observed in Fig. 6a for silk G-MoS<sub>2</sub> nanocomposite. After passing through the holes in the valence band (VB) of the material, the charged electrons travel to the conduction band (CB). Due to the electron-hole partitioning caused by photo-induced electrons captured from silk G, the recombination process was slowed down. The redox reaction was taken up in

the MoS<sub>2</sub>/Silk G nanocomposites solution. The hydroxyl radical is generated due to the oxidation of hole by water molecules which was present above the layer of MoS<sub>2</sub>/Silk G nanomaterials. Anionic superoxide radicals are developed when oxygen absorbs the stimulated electron in conduction band of MoS<sub>2</sub>/Silk G nanocomposites, which subsequently produces incredibly reactive hydroxyl radicals (OH<sup>•</sup>) after being combined with a proton to produce O<sub>2</sub>H<sup>•</sup>. By interacting with the aromatic ring, breaking up the azo link and hydroxylating the ring, the OH<sup>•</sup> is broken down by methylene blue to create CO<sub>2</sub>, H<sub>2</sub>O, SO<sub>4</sub><sup>2-</sup>, NO<sub>3</sub><sup>-</sup> and NH<sub>4</sub><sup>+</sup> ions. Fig. 7 illustrates the potential means for photocatalytic degeneration of organic dye made using MoS<sub>2</sub>/Silk G nanobiocomposite.

The electrocatalytic OER characteristics of the as-synthesized materials were assessed using a three-electrode setup. The LSV curves of MoS<sub>2</sub> and MoS<sub>2</sub>/Silk G (Fig. 8a) clearly indicates that the MoS<sub>2</sub>/Silk G requires lower over-potential than pure MoS<sub>2</sub>, which is due to the highly conductive structure of silk MoS<sub>2</sub>. The MoS<sub>2</sub> and MoS<sub>2</sub> silk show an overpotential of 608 mV *vs.* Ag/AgCl (865 mV *vs.* RHE) and 855 mV *vs.* Ag/AgCl (1.112 V *vs.* RHE) operating at the current density of 10 mA cm<sup>-2</sup>, respectively. The MoS<sub>2</sub> silk composite indicates a lower Tafel slope of 157.2 mV dec<sup>-1</sup> than MoS<sub>2</sub> (165.2 mV dec<sup>-1</sup>) (Fig. 8b), which indicate that the higher electrochemical activity of MoS<sub>2</sub> silk are because of higher band gap [42,43].

**Electrochemical studies:** The synthesized nanobiocomposite silk G/MoS<sub>2</sub> shows the better electrochemical perfor-

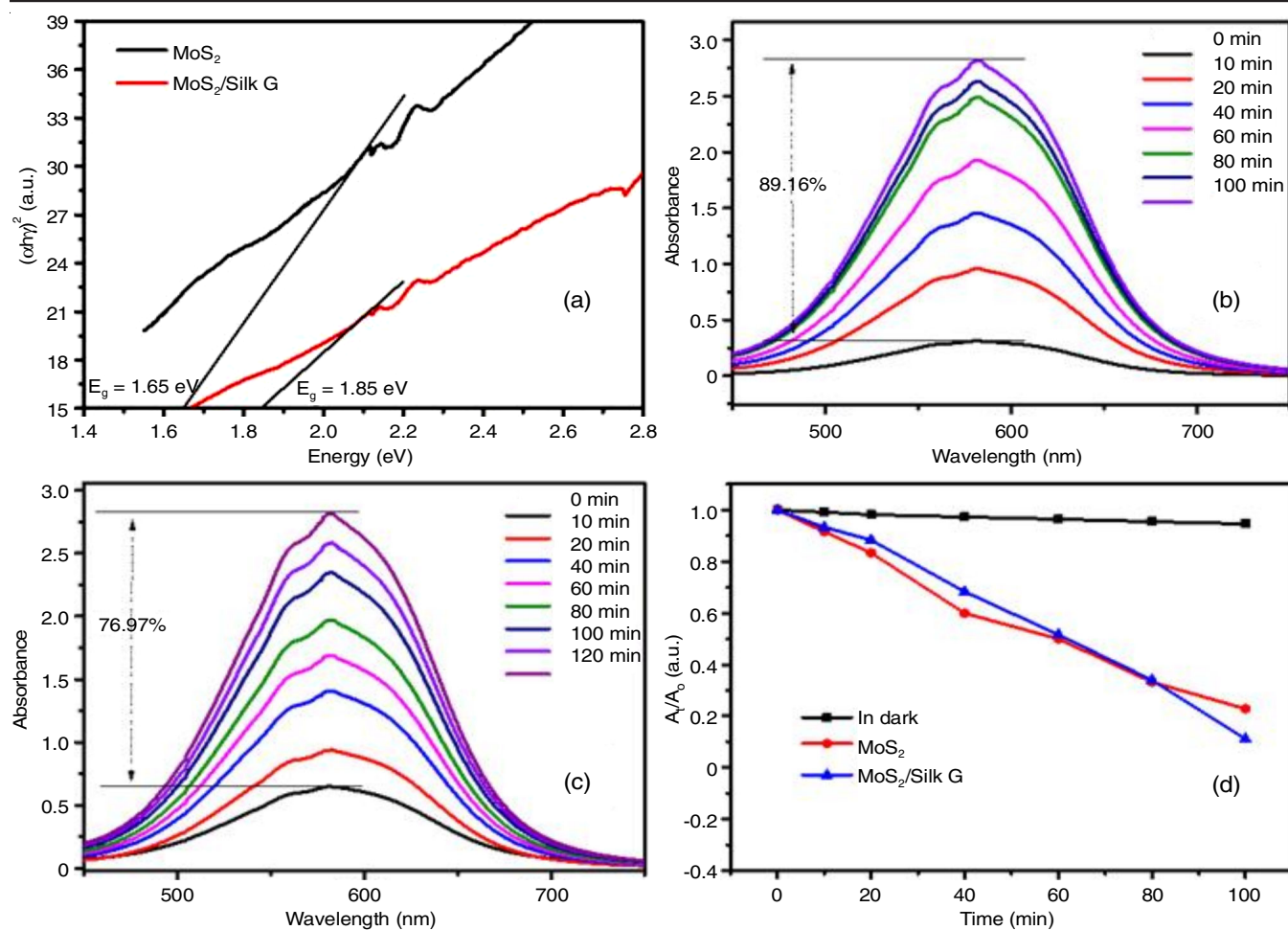


Fig. 6. (a) UV-vis spectrum band gap of MoS<sub>2</sub> & MoS<sub>2</sub>/silk G nanocomposites, (b, c & d) photocatalytic disintegration of organic dye utilizing MoS<sub>2</sub> & MoS<sub>2</sub>/silk G nanocomposites

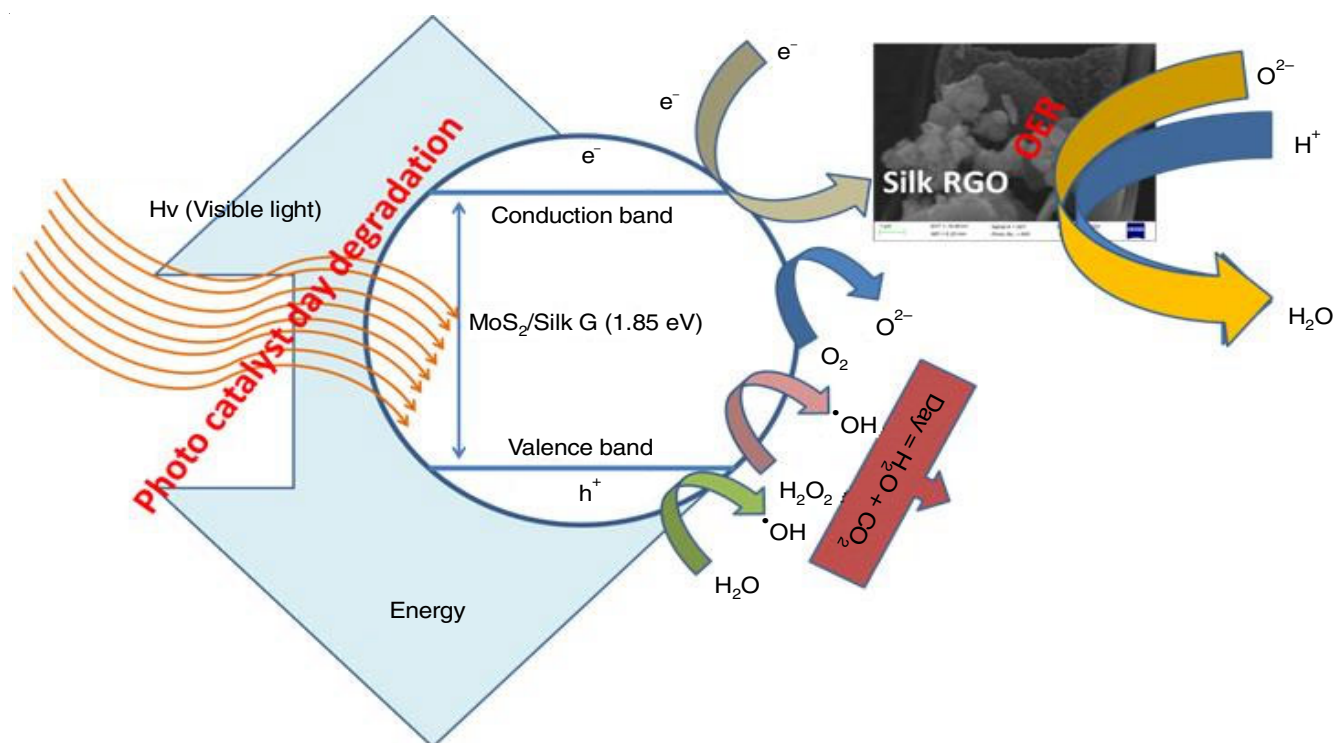


Fig. 7. A plausible mechanism for the OER and photocatalytic degradation of organic dye utilizing MoS<sub>2</sub>/Silk G nanocomposites

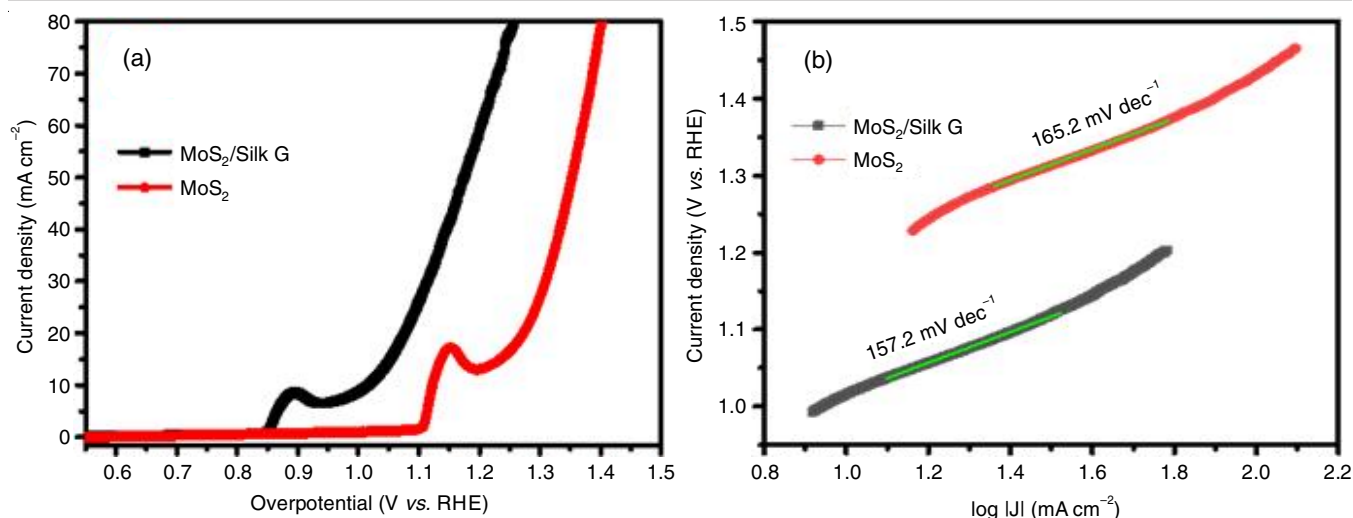


Fig. 8. (a) LSV curves, (b) Tafel plots of MoS<sub>2</sub> and MoS<sub>2</sub>/Silk G nanocomposite

mance than most of the reported catalysts as shown in Table-1, moreover, stability is another crucial parameter for an electrocatalyst. The stability of the samples has been assessed through cyclic voltammetry curves for 800 cycles. The CV curves of the sample up to 800 cycles are shown in Fig. 9. The negligible change in the current density values at 0.95 V for both samples indicates the high cyclic stability of the samples.

To estimate the electrochemical active surface area (ECSA), the CV curves were recorded at varied scan rates. The CV curves of MoS<sub>2</sub> silk and pure MoS<sub>2</sub> are shown in Fig. 10a-b. The electrochemical double layer capacitance ( $C_{dl}$ ) is directly proportional to the effective surface area (ECSA). MoS<sub>2</sub> silk signifies the increased ECSA content of 0.30 mF cm<sup>-2</sup> than the pure MoS<sub>2</sub> (0.24 mF cm<sup>-2</sup>) sample that are in well accord for our LSV findings (Fig. 10c). To get more understanding of the electrochemical mechanism of samples, the electrochemical impedance spectroscopy (EIS) has been investigated. From the Nyquist plots of the samples (Fig. 10d), MoS<sub>2</sub> silk composite possesses smaller semicircle than pure MoS<sub>2</sub>, which indicates the low  $R_{ct}$  value [11]. The lower charge transfer resistance of MoS<sub>2</sub> silk is responsible for high electrochemical performance.

TABLE-1  
COMPARISON OF MoS<sub>2</sub>/SILK G WITH  
OTHER REPORTED ELECTROCATALYSTS

Catalyst	Electrolyte	Tafel slope (mV dec <sup>-1</sup> )	Ref.
MoS <sub>2</sub> /Slik G	1 M KOH	157.2	This work
Commercial RuO <sub>2</sub>	0.1 M HClO <sub>4</sub>	69.5	[44]
Co-B NS/G	1 M KOH	160.0	[45]
BiVO <sub>4</sub>	0.5 M KOH	221.0	[46]
13X/PANI-15	1 M KOH	168.0	[47]
NiO(OH)	KOH solution	180.0	[48]
NiCo(OH) <sub>x</sub>	1 M KOH	109.0	[49]
FeP-rGO (50:50) on carbon fiber paper	1 M KOH	174.9	[50]
Cu metal-organic framework (MOF)	0.5 M H <sub>2</sub> SO <sub>4</sub>	211.0	[51]

## Conclusion

To summarize, the supercritical fluids and chemical vapor deposition (CVD) techniques to fabricate a MoS<sub>2</sub> and silk G composite as photocatalytic materials. The prepared composite was characterized for there structure and morphology using XRD, TEM, SEM and FTIR techniques. Furthermore, the

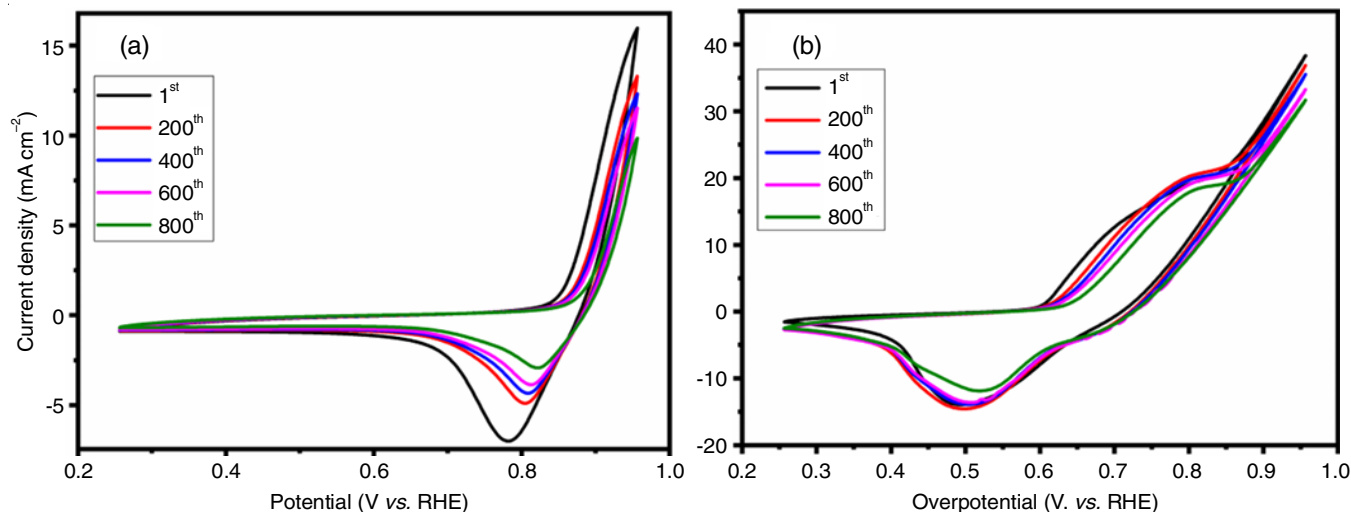


Fig. 9. CV curves up to 800 cycles of (a) MoS<sub>2</sub> and (b) MoS<sub>2</sub>/Silk G nanocomposite

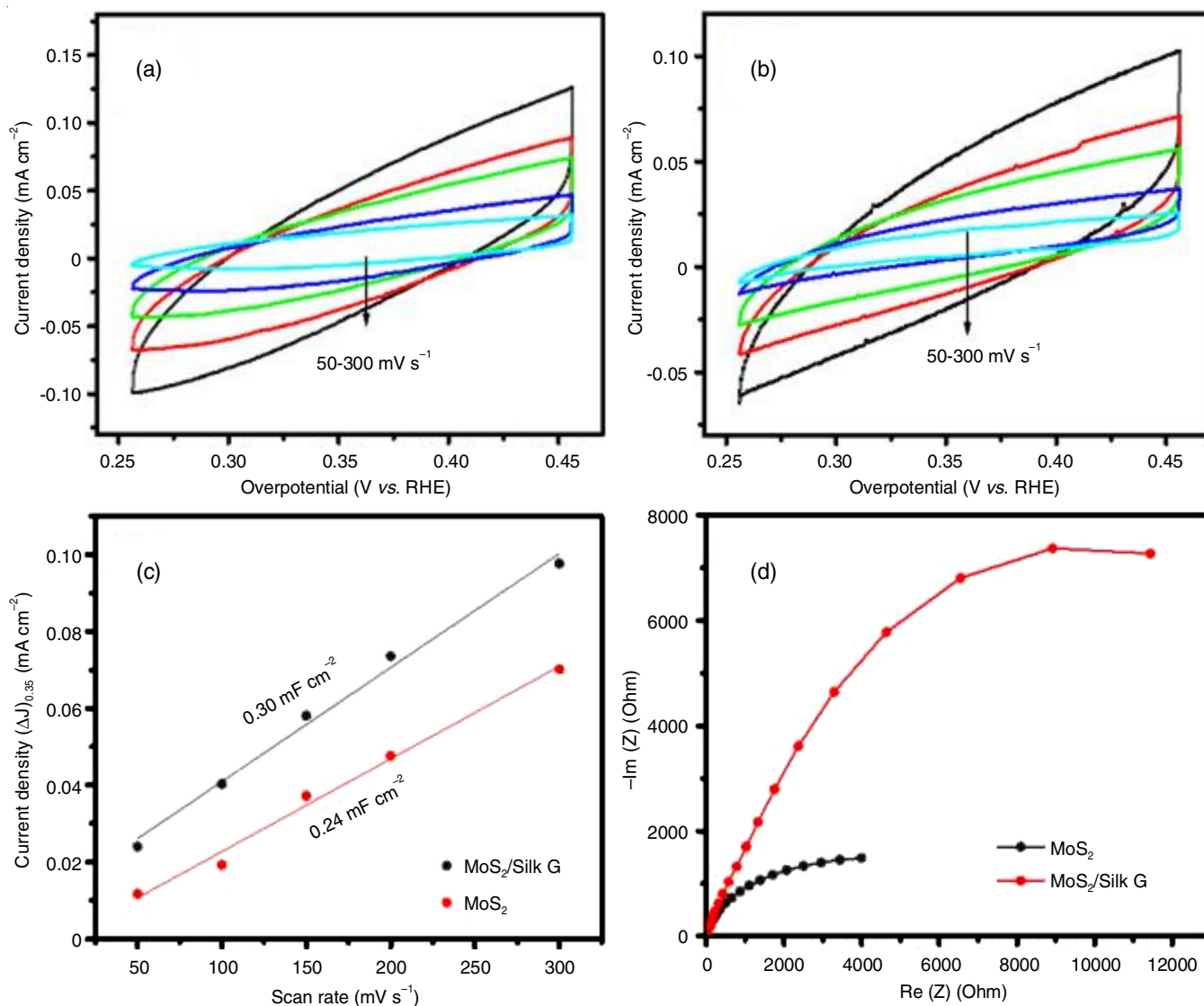


Fig. 10. Cyclic voltammograms at various scan rates of (a) MoS<sub>2</sub>/Silk G and (b) MoS<sub>2</sub>, (c) C<sub>dl</sub> values and (d) Nyquist plots of MoS<sub>2</sub> and MoS<sub>2</sub>/Silk G composite

optical properties of MoS<sub>2</sub>/Silk G composite were enhanced with the implementation of silk G, resulting in a modification of the band gap, which increased to 1.85 eV. This enhanced bandgap would have a significant impact on generating an increased number of electron-hole pairs under visible light. Therefore, silk G improves the rapid mobility of photo-induced charge entities by suppressing the recombination process. Also, it exhibits high electrocatalytic reaction, in addition to low over potential of 603 mV defined with 10 mA cm<sup>-2</sup> current density and low Tafel slope of 157.2 mV dec<sup>-1</sup>. Thus, the incorporation of silk G into the MoS<sub>2</sub> host resulted in a 13% increase in photocatalytic property and a nearly 5% increase in electrocatalytic activity compared to MoS<sub>2</sub> nanoparticles.

#### ACKNOWLEDGEMENTS

The authors sincerely thank Uttaranchal University for the material testing and ATME college of Engineering for financial support under the research incentive scheme.

#### CONFLICT OF INTEREST

The authors declare that there is no conflict of interests regarding the publication of this article.

#### REFERENCES

1. Y. Dahiya, M. Hariram, M. Kumar, A. Jain and D. Sarkar, *Coord. Chem. Rev.*, **451**, 214265 (2022); <https://doi.org/10.1016/j.ccr.2021.214265>
2. K.C. Kwon, J.H. Baek, K. Hong, S.Y. Kim and H.W. Jang, *Nano-Micro Lett.*, **14**, 58 (2022); <https://doi.org/10.1007/s40820-021-00784-3>
3. J. Hong, X. Chen, P. Li, M. Koshino, S. Li, H. Xu, Z. Hu, F. Ding and K. Suenaga, *Adv. Mater.*, **34**, 2200643 (2022); <https://doi.org/10.1002/adma.202200643>
4. K.C. Kwon, J.H. Baek, K. Hong, S.Y. Kim and H.W. Jang, *Nano-Micro Lett.*, **14**, 58 (2022); <https://doi.org/10.1007/s40820-021-00784-3>
5. G. Halligudra, C.C. Paramesh, R. Gururaj, D. Rangappa, A. Giridasappa, C. Sabbanahalli, A.K.C. Siddegowda, A.K.M. Raghunathareddy and P.D. Shivaramu, *Ceram. Int.*, **48**, 35698 (2022); <https://doi.org/10.1016/j.ceramint.2022.06.188>

6. R. Mudike, C. Sabbanahalli, J.B. Sriramoju, A. Bheemaraju, G. Halligudra, M. Muniyappa, M.P. Narayanaswamy, A.K. Cs, P.D. Shivaramu and D. Rangappa, *Mater. Res. Bull.*, **146**, 111606 (2022); <https://doi.org/10.1016/j.materresbull.2021.111606>
7. J.B. Sriramoju, M. Muniyappa, N.R. Marilingaiah, C. Sabbanahalli, M. Shetty, R. Mudike, C.P. Chitrabanu, P.D. Shivaramu, G. Nagaraju, K.S. Rangappa, C.S. Ananda Kumar and D. Rangappa, *Ceram. Int.*, **47**, 10321 (2021); <https://doi.org/10.1016/j.ceramint.2020.12.014>
8. S. Upadhyay and O.P. Pandey, *J. Energy Storage*, **40**, 102809 (2021); <https://doi.org/10.1016/j.est.2021.102809>
9. S. Upadhyay and O.P. Pandey, *J. Power Sources*, **535**, 231450 (2022); <https://doi.org/10.1016/j.jpowsour.2022.231450>
10. S. Wang, L. Liao, Z. Shi, J. Xiao, Q. Gao, Y. Zhang, B. Liu and Y. Tang, *ChemElectroChem*, **3**, 2110 (2016); <https://doi.org/10.1002/celec.201600325>
11. S. Upadhyay and O.P. Pandey, *Electrochim. Acta*, **412**, 140109 (2022); <https://doi.org/10.1016/j.electacta.2022.140109>
12. S. Upadhyay and O.P. Pandey, *J. Electrochem. Soc.*, **169**, 016511 (2022); <https://doi.org/10.1149/1945-7111/ac4a52>
13. X. Pang, T. Wu, Y. Gu, D. Wang, X. Che, D. Sun and F. Huang, *Chem. Commun.*, **56**, 9036 (2020); <https://doi.org/10.1039/D0CC03282D>
14. P. Baskaran, K.D. Nisha, S. Harish, H. Ikeda, J. Archana and M. Navaneethan, *J. Alloys Compd.*, **894**, 162166 (2022); <https://doi.org/10.1016/j.jallcom.2021.162166>
15. C. Sabanahalli, K. Roy, M.P. Kumar, R. Mudike, C.S. Ananda Kumar, P.D. Shivaramu, K.G.B. Kumar, N. Basavegowda and D. Rangappa, *Ceram. Int.*, **48**, 35860 (2022); <https://doi.org/10.1016/j.ceramint.2022.08.104>
16. J. Swapnalin, P. Banerjee, C. Sabbanahalli, D. Rangappa and K.K. Kondamareddy, Computational Techniques on Optical Properties of Metal-Oxide Semiconductors, In: Optical Properties and Applications of Semiconductors, CRC Press, pp. 155–166 (2022).
17. P. Choudhary, A. Pathak, P. Kumar, S. Chetana and N. Sharma, *Biomass Conv. Bioref.* (2022); <https://doi.org/10.1007/s13399-022-03145-1>
18. N.C. Joshi, B.S. Rawat, H. Bisht, V. Gajraj, N. Kumar, S. Chetana and P. Gururani, *Synth. Met.*, **289**, 117132 (2022); <https://doi.org/10.1016/j.synthmet.2022.117132>
19. Q. Lu, Y. Yu, Q. Ma, B. Chen, H. Zhang, Q. Lu, Y. Yu, Q. Ma, B. Chen and H. Zeng, *Adv. Mater.*, **28**, 1917 (2016); <https://doi.org/10.1002/adma.201503270>
20. A. Joseph and P.M. Aneesh, *Mater. Res. Bull.*, **146**, 111623 (2022); <https://doi.org/10.1016/j.materresbull.2021.111623>
21. S. Palchoudhury, K. Ramasamy and A. Gupta, *Nanoscale Adv.*, **2**, 3069 (2020); <https://doi.org/10.1039/D0NA000399A>
22. J. Zhou, Y. Cheng and Y. Zhu, *Adv. Mater. Interfaces*, **9**, 2102334 (2022); <https://doi.org/10.1002/admi.202102334>
23. G. Rani, J. Rajesh Banu and K.N. Yogalakshmi, Electrode Modification and its Application in Microbial Electrolysis Cell, In: Scaling Up of Microbial Electrochemical Systems: From Reality to Scalability, Elsevier, pp. 339–357 (2022); <https://doi.org/10.1016/B978-0-323-90765-1.00018-6>
24. M. Kumar, B.E. Kumara Swamy, S. Reddy, W. Zhao, S. Chetana and V. Gowrav Kumar, *J. Electroanal. Chem.*, **835**, 96 (2019); <https://doi.org/10.1016/j.jelechem.2019.01.019>
25. F.M. Sapountzi, J.M. Gracia, C.J. (Kees-Jan) Weststrate, H.O.A. Fredriksson and J.W. (Hans) Niemantsverdriet, *Progr. Energy Combust. Sci.*, **58**, 1 (2017). <https://doi.org/10.1016/j.peccs.2016.09.001>
26. M. Shastri, M. Shetty, N. Rani, M. Muniyappa, V. Gangaraju, M.S. Sree, V. Gangaraju, C. Sabanahalli, S.V. Lokesh, P.D. Shivaramu and D. Rangappa, *Ceram. Int.*, **47**, 14790 (2021); <https://doi.org/10.1016/j.ceramint.2020.10.215>
27. W.S. Su and C.H. Yeh, *Diamond Rel. Mater.*, **124**, 108897 (2022); <https://doi.org/10.1016/j.diamond.2022.108897>
28. B. Han and Y.H. Hu, *J. Phys. Chem. C*, **119**, 18927 (2015); <https://doi.org/10.1021/acs.jpcc.5b04894>
29. N. Kumar, A.S. Bhadwal, B. Mizaiakoff, S. Singh and C. Kranz, *Sens. Biosensing Res.*, **24**, 100288 (2019); <https://doi.org/10.1016/j.sbsr.2019.100288>
30. P.O. Agboola and I. Shakir, *J. Mater. Res. Technol.*, **18**, 4303 (2022); <https://doi.org/10.1016/j.jmrt.2022.04.109>
31. D. Liu, Z. Lv, J. Dang, W. Ma, K. Jian, M. Wang, D. Huang and W. Tian, *Inorg. Chem.*, **60**, 9932 (2021); <https://doi.org/10.1021/acs.inorgchem.1c01193>
32. E. Benavente, F. Durán, C. Sotomayor-Torres and G. González, *J. Phys. Chem. Solids*, **113**, 119 (2018); <https://doi.org/10.1016/j.jpcs.2017.10.027>
33. Q. Liu, H. Zhu, Q. Ma, M. Liu, B. Wang, C. Tang, Y. Wang, Q. Wu, X. Wang and Z. Hu, *FlatChem*, **26**, 100212 (2021); <https://doi.org/10.1016/j.flatc.2020.100212>
34. H. Xie and X. Xiong, *J. Environ. Chem. Eng.*, **5**, 1150 (2017); <https://doi.org/10.1016/j.jece.2017.01.044>
35. M. Nishita, S.-Y. Park, T. Nishio, K. Kamizaki, Z.C. Wang, K. Tamada, T. Takumi, R. Hashimoto, H. Otani, G.J. Pazour, V.W. Hsu and Y. Minami, *Sci. Rep.*, **7**, 1 (2017); <https://doi.org/10.1038/s41598-016-0028-x>
36. S. Chetana, V.N. Thakur, N. Kumar, N.C. Joshi, S. Upadhyay, K. Roy, K.G.B. Kumar and D. Rangappa, *J. Mater. Sci. Mater. Electron.*, **34**, 1886 (2023); <https://doi.org/10.1007/s10854-023-11267-z>
37. M. Shetty, C. Schübler, M. Shastri, C. Sabbanahalli, C.P. Chitrabanu, M. Murthy, S. Jagadeesh Babu, T. Tomai, K.S. Anantharaju, P.D. Shivaramu and D. Rangappa, *Ceram. Int.*, **47**, 10274 (2021); <https://doi.org/10.1016/j.ceramint.2020.12.061>
38. L. Li, H. Bi, S. Gai, F. He, P. Gao, Y. Dai, X. Zhang, D. Yang, M. Zhang and P. Yang, *Sci. Rep.*, **7**, 43116 (2017); <https://doi.org/10.1038/srep43116>
39. L. Ge, C. Han, X. Xiao and L. Guo, *Int. J. Hydrogen Energy*, **38**, 6960 (2013); <https://doi.org/10.1016/j.ijhydene.2013.04.006>
40. H.M. El Sharkawy, A.S. Dhmees, A.R. Tamman, S.M. El Sabagh, R.M. Aboushabha and N.K. Allam, *J. Energy Storage*, **27**, 101078 (2020); <https://doi.org/10.1016/j.est.2019.101078>
41. J.H. Fan, P. Gao, A.M. Zhang, B.R. Zhu, H.L. Zeng, X.D. Cui, R. He and Q.M. Zhang, *J. Appl. Phys.*, **115**, 053527 (2014); <https://doi.org/10.1063/1.4862859>
42. S. Upadhyay and O.P. Pandey, *Int. J. Hydrogen Energy*, **45**, 27114 (2020); <https://doi.org/10.1016/j.ijhydene.2020.07.069>
43. L. González-Reyes, I. Hernández-Perez, L. Díaz-Barriga Arceo and A. Manzo-Robledo, *Mater. Sci. Forum*, **691**, 105 (2011); <https://doi.org/10.4028/www.scientific.net/MSF.691.105>
44. L. Zhang, H. Jang, H. Liu, M. G. Kim, D. Yang, S. Liu, X. Liu and J. Cho, *Angew. Chem. Int. Ed.*, **60**, 18821 (2021); <https://doi.org/10.1002/anie.202106631>
45. P. Chen, K. Xu, T. Zhou, Y. Tong, J. Wu, H. Cheng, X. Lu, H. Ding, C. Wu, Y. Xie, P. Z. Chen, K. Xu, T. P. Zhou, Y. Tong, J. C. Wu, X. L. Lu, H. Ding, C. Z. Wu and Y. Xie, *Angew. Chem. Int. Ed.*, **55**, 2488 (2016); <https://doi.org/10.1002/anie.201511032>
46. R.A. Mir and O.P. Pandey, *Appl. Phys. Lett.*, **118**, 253902 (2021); <https://doi.org/10.1063/5.0057082>
47. R. Vinodh, C. Deviprasath, C. V. V. Muralee Gopi, V. G. Raghavendra Kummara, R. Atchudan, T. Ahamad, H.J. Kim and M. Yi, *Int. J. Hydrogen Energy*, **45**, 28337 (2020); <https://doi.org/10.1016/j.ijhydene.2020.07.194>
48. I. Arulraj and D.C. Trivedi, *Int. J. Hydrogen Energy*, **14**, 893 (1989); [https://doi.org/10.1016/0360-3199\(89\)90076-1](https://doi.org/10.1016/0360-3199(89)90076-1)
49. J. Nai, H. Yin, T. You, L. Zheng, J. Zhang, P. Wang, Z. Jin, Y. Tian, J. Liu, Z. Tang and L. Guo, *Adv. Energy Mater.*, **5**, 1401880 (2015); <https://doi.org/10.1002/aenm.201401880>
50. J. Masud, S. Umapathi, N. Ashokaan and M. Nath, *J. Mater. Chem. A*, **4**, 9750 (2016); <https://doi.org/10.1039/C6TA04025J>
51. M. Jahan, Z. Liu and K.P. Loh, *Adv. Funct. Mater.*, **23**, 5363 (2013); <https://doi.org/10.1002/adfm.201300510>